*K[superscript *0] production in Cu + Cu and Au + Au collisions at √s[subscript NN]=62.4 GeV and 200 GeV*

K^{*0} production in Cu + Cu and Au + Au collisions at $\sqrt{s_{NN}} = 62.4$ GeV and 200 GeV

M. M. Aggarwal,[31] Z. Ahammed,[22] A. V. Alakhverdyants,[18] I. Alekseev,[16] J. Alford,[19] B. D. Anderson,[19] C. D. Anson,[29] D. Arkhipkin,[3] G. S. Averichev,[18] J. Balewski,[23] L. S. Barnby,[2] S. Baumgart,[53] D. R. Beavis,[3] R. Bellwied,[51] M. J. Betancourt,[23] R. R. Betts,[8] A. Bhasin,[17] A. K. Bhati,[31] H. Bichsel,[50] J. Bielcik,[10] J. Bielcikova,[11] B. Biritz,[6] L. C. Bland,[3] B. E. Bonner,[37] J. Bouchet,[19] E. Braidot,[28] A. V. Brandin,[26] A. Bridgeman,[1] E. Bruna,[53] S. Bueltmann,[30] I. Bunzarov,[18] T. P. Burton,[3] X. Z. Cai,[41] H. Caines,[53] M. Calderon de la Barca Sanchez,[5] O. Catu,[53] D. Cebra,[5] R. Cendejas,[6] M. C. Cervantes,[43] Z. Chajecki,[29] P. Chaloupka,[11] S. Chattopadhyay,[48] H. F. Chen,[39] J. H. Chen,[41] J. Y. Chen,[52] J. Cheng,[45] M. Cherney,[9] A. Chikanian,[53] K. E. Choi,[35] W. Christie,[3] P. Chung,[11] R. F. Clarke,[43] M. J. M. Codrington,[43] R. Corliss,[23] J. G. Cramer,[50] H. J. Crawford,[4] D. Das,[5] S. Dash,[13] A. Davila Leyva,[44] L. C. De Silva,[51] R. R. Debbe,[3] T. G. Dedovich,[18] A. A. Derevschikov,[33] R. Derradi de Souza,[7] L. Didenko,[3] P. Djawotho,[43] S. M. Dogra,[17] X. Dong,[22] J. L. Drachenberg,[43] J. E. Draper,[5] J. C. Dunlop,[3] M. R. Dutta Mazumdar,[48] L. G. Efimov,[18] E. Elhalhuli,[2] M. Elnimr,[51] J. Engelage,[4] G. Eppley,[37] B. Erazmus,[42] M. Estienne,[42] L. Eun,[32] O. Evdokimov,[8] P. Fachini,[3] R. Fatemi,[20] J. Fedorisin,[18] R. G. Fersch,[20] P. Filip,[18] E. Finch,[53] V. Fine,[3] Y. Fisyak,[3] C. A. Gagliardi,[43] D. R. Gangadharan,[6] M. S. Ganti,[48] E. J. Garcia-Solis,[8] A. Geromitsos,[42] F. Geurts,[37] V. Ghazikhanian,[6] P. Ghosh,[48] Y. N. Gorbunov,[9] A. Gordon,[3] O. Grebenyuk,[22] D. Grosnick,[47] S. M. Guertin,[6] A. Gupta,[17] W. Guryn,[3] B. Haag,[5] A. Hamed,[43] L.-X. Han,[41] J. W. Harris,[53] J. P. Hays-Wehle,[23] M. Heinz,[53] S. Heppelmann,[32] A. Hirsch,[34] E. Hjort,[22] A. M. Hoffman,[23] G. W. Hoffmann,[44] D. J. Hofman,[8] B. Huang,[39] H. Z. Huang,[6] T. J. Humanic,[29] L. Huo,[43] G. Igo,[6] P. Jacobs,[22] W. W. Jacobs,[15] C. Jena,[13] F. Jin,[41] C. L. Jones,[23] P. G. Jones,[2] J. Joseph,[19] E. G. Judd,[4] S. Kabana,[42] K. Kajimoto,[44] K. Kang,[45] J. Kapitan,[11] K. Kauder,[8] D. Keane,[19] A. Kechechyan,[18] D. Kettler,[50] D. P. Kikola,[22] J. Kiryluk,[22] A. Kisiel,[49] S. R. Klein,[22] A. G. Knospe,[53] A. Kocoloski,[23] D. D. Koetke,[47] T. Kollegger,[12] J. Konzer,[34] I. Koralt,[30] L. Koroleva,[16] W. Korsch,[20] L. Kotchenda,[26] V. Kouchpil,[11] P. Kravtsov,[26] K. Krueger,[1] M. Krus,[10] L. Kumar,[19] P. Kurnadi,[6] M. A. C. Lamont,[3] J. M. Landgraf,[3] S. LaPointe,[51] J. Lauret,[3] A. Lebedev,[3] R. Lednicky,[18] C.-H. Lee,[35] J. H. Lee,[3] W. Leight,[23] M. J. LeVine,[3] C. Li,[39] L. Li,[44] N. Li,[52] W. Li,[41] X. Li,[34] X. Li,[40] Y. Li,[45] Z. M. Li,[52] G. Lin,[53] S. J. Lindenbaum,[27] M. A. Lisa,[29] F. Liu,[52] H. Liu,[5] J. Liu,[37] T. Ljubicic,[3] W. J. Llope,[37] R. S. Longacre,[3] W. A. Love,[3] Y. Lu,[39] E. V. Lukashov,[26] X. Luo,[39] G. L. Ma,[41] Y. G. Ma,[41] D. P. Mahapatra,[13] R. Majka,[53] O. I. Mall,[5] L. K. Mangotra,[17] R. Manweiler,[47] S. Margetis,[19] C. Markert,[44] H. Masui,[22] H. S. Matis,[22] Yu. A. Matulenko,[33] D. McDonald,[37] T. S. McShane,[9] A. Meschanin,[33] R. Milner,[23] N. G. Minaev,[33] S. Mioduszewski,[43] A. Mischke,[28] M. K. Mitrovski,[12] B. Mohanty,[48] M. M. Mondal,[48] B. Morozov,[16] D. A. Morozov,[33] M. G. Munhoz,[38] B. K. Nandi,[14] C. Nattrass,[53] T. K. Nayak,[48] J. M. Nelson,[2] P. K. Netrakanti,[34] M. J. Ng,[4] L. V. Nogach,[33] S. B. Nurushev,[33] G. Odyniec,[22] A. Ogawa,[3] V. Okorokov,[26] E. W. Oldag,[44] D. Olson,[22] M. Pachr,[10] B. S. Page,[15] S. K. Pal,[48] Y. Pandit,[19] Y. Panebratsev,[18] T. Pawlak,[49] T. Peitzmann,[28] V. Perevoztchikov,[3] C. Perkins,[4] W. Peryt,[49] S. C. Phatak,[13] P. Pile,[3] M. Planinic,[54] M. A. Ploskon,[22] J. Pluta,[49] D. Plyku,[30] N. Poljak,[54] A. M. Poskanzer,[22] B. V. K. S. Potukuchi,[17] C. B. Powell,[22] D. Prindle,[50] C. Pruneau,[51] N. K. Pruthi,[31] P. R. Pujahari,[14] J. Putschke,[53] H. Qiu,[21] R. Raniwala,[36] S. Raniwala,[36] R. L. Ray,[44] R. Redwine,[23] R. Reed,[5] H. G. Ritter,[22] J. B. Roberts,[37] O. V. Rogachevskiy,[18] J. L. Romero,[5] A. Rose,[22] C. Roy,[42] L. Ruan,[3] R. Sahoo,[42] S. Sakai,[6] I. Sakrejda,[22] T. Sakuma,[23] S. Salur,[5] J. Sandweiss,[53] E. Sangaline,[5] J. Schambach,[44] R. P. Scharenberg,[34] N. Schmitz,[24] T. R. Schuster,[12] J. Seele,[23] J. Seger,[9] I. Selyuzhenkov,[15] P. Seyboth,[24] E. Shahaliev,[18] M. Shao,[39] M. Sharma,[51] S. S. Shi,[52] E. P. Sichtermann,[22] F. Simon,[24] R. N. Singaraju,[48] M. J. Skoby,[34] N. Smirnov,[53] P. Sorensen,[3] J. Sowinski,[15] H. M. Spinka,[1] B. Srivastava,[34] T. D. S. Stanislaus,[47] D. Staszak,[6] J. R. Stevens,[15] R. Stock,[12] M. Strikhanov,[26] B. Stringfellow,[34] A. A. P. Suaide,[38] M. C. Suarez,[8] N. L. Subba,[19] M. Sumbera,[11] X. M. Sun,[22] Y. Sun,[39] Z. Sun,[21] B. Surrow,[23] D. N. Svirida,[16] T. J. M. Symons,[22] A. Szanto de Toledo,[38] J. Takahashi,[7] A. H. Tang,[3] Z. Tang,[39] L. H. Tarini,[51] T. Tarnowsky,[25] D. Thein,[44] J. H. Thomas,[22] J. Tian,[41] A. R. Timmins,[51] S. Timoshenko,[26] D. Tlusty,[11] M. Tokarev,[18] T. A. Trainor,[50] V. N. Tram,[22] S. Trentalange,[6] R. E. Tribble,[43] O. D. Tsai,[6] J. Ulery,[34] T. Ullrich,[3] D. G. Underwood,[1] G. Van Buren,[3] M. van Leeuwen,[28] G. van Nieuwenhuizen,[23] J. A. Vanfossen Jr.,[19] R. Varma,[14] G. M. S. Vasconcelos,[7] A. N. Vasiliev,[33] F. Videbaek,[3] Y. P. Viyogi,[48] S. Vokal,[18] S. A. Voloshin,[51] M. Wada,[44] M. Walker,[23] F. Wang,[34] G. Wang,[6] H. Wang,[25] J. S. Wang,[21] Q. Wang,[34] X. L. Wang,[39] Y. Wang,[45] G. Webb,[20] J. C. Webb,[3] G. D. Westfall,[25] C. Whitten Jr.,[6] H. Wieman,[22] S. W. Wissink,[15] R. Witt,[46] Y. F. Wu,[52] W. Xie,[34] H. Xu,[21] N. Xu,[22] Q. H. Xu,[40] W. Xu,[6] Y. Xu,[39] Z. Xu,[3] L. Xue,[41] Y. Yang,[21] P. Yepes,[37] K. Yip,[3] I.-K. Yoo,[35] Q. Yue,[45] M. Zawisza,[49] H. Zbroszczyk,[49] W. Zhan,[21] J. B. Zhang,[52] S. Zhang,[41] W. M. Zhang,[9] X. P. Zhang,[22] Y. Zhang,[22] Z. P. Zhang,[39] J. Zhao,[41] C. Zhong,[41] J. Zhou,[37] W. Zhou,[40] X. Zhu,[45] Y. H. Zhu,[41] R. Zoulkarneev,[18] and Y. Zoulkarneeva[18]

(STAR Collaboration)

[1]*Argonne National Laboratory, Argonne, Illinois 60439, USA*
[2]*University of Birmingham, Birmingham, United Kingdom*
[3]*Brookhaven National Laboratory, Upton, New York 11973, USA*
[4]*University of California, Berkeley, California 94720, USA*
[5]*University of California, Davis, California 95616, USA*
[6]*University of California, Los Angeles, California 90095, USA*
[7]*Universidade Estadual de Campinas, Sao Paulo, Brazil*
[8]*University of Illinois at Chicago, Chicago, Illinois 60607, USA*
[9]*Creighton University, Omaha, Nebraska 68178, USA*

[10]*Czech Technical University in Prague, FNSPE, Prague CZ-11519, Czech Republic*
[11]*Nuclear Physics Institute AS CR, CZ-25068 Řež/Prague, Czech Republic*
[12]*University of Frankfurt, Frankfurt, Germany*
[13]*Institute of Physics, Bhubaneswar 751005, India*
[14]*Indian Institute of Technology, Mumbai, India*
[15]*Indiana University, Bloomington, Indiana 47408, USA*
[16]*Alikhanov Institute for Theoretical and Experimental Physics, Moscow, Russia*
[17]*University of Jammu, Jammu 180001, India*
[18]*Joint Institute for Nuclear Research, Dubna 141 980, Russia*
[19]*Kent State University, Kent, Ohio 44242, USA*
[20]*University of Kentucky, Lexington, Kentucky 40506-0055, USA*
[21]*Institute of Modern Physics, Lanzhou, China*
[22]*Lawrence Berkeley National Laboratory, Berkeley, California 94720, USA*
[23]*Massachusetts Institute of Technology, Cambridge, Massachusetts 02139-4307, USA*
[24]*Max-Planck-Institut für Physik, Munich, Germany*
[25]*Michigan State University, East Lansing, Michigan 48824, USA*
[26]*Moscow Engineering Physics Institute, Moscow, Russia*
[27]*City College of New York, New York City, New York 10031, USA*
[28]*NIKHEF and Utrecht University, Amsterdam, The Netherlands*
[29]*Ohio State University, Columbus, Ohio 43210, USA*
[30]*Old Dominion University, Norfolk, Virginia 23529, USA*
[31]*Panjab University, Chandigarh 160014, India*
[32]*Pennsylvania State University, University Park, Pennsylvania 16802, USA*
[33]*Institute of High Energy Physics, Protvino, Russia*
[34]*Purdue University, West Lafayette, Indiana 47907, USA*
[35]*Pusan National University, Pusan, Republic of Korea*
[36]*University of Rajasthan, Jaipur 302004, India*
[37]*Rice University, Houston, Texas 77251, USA*
[38]*Universidade de Sao Paulo, Sao Paulo, Brazil*
[39]*University of Science & Technology of China, Hefei 230026, China*
[40]*Shandong University, Jinan, Shandong 250100, China*
[41]*Shanghai Institute of Applied Physics, Shanghai 201800, China*
[42]*SUBATECH, Nantes, France*
[43]*Texas A&M University, College Station, Texas 77843, USA*
[44]*University of Texas, Austin, Texas 78712, USA*
[45]*Tsinghua University, Beijing 100084, China*
[46]*United States Naval Academy, Annapolis, Maryland 21402, USA*
[47]*Valparaiso University, Valparaiso, Indiana 46383, USA*
[48]*Variable Energy Cyclotron Centre, Kolkata 700064, India*
[49]*Warsaw University of Technology, Warsaw, Poland*
[50]*University of Washington, Seattle, Washington 98195, USA*
[51]*Wayne State University, Detroit, Michigan 48201, USA*
[52]*Institute of Particle Physics, CCNU (HZNU), Wuhan 430079, China*
[53]*Yale University, New Haven, Connecticut 06520, USA*
[54]*University of Zagreb, Zagreb HR-10002, Croatia*

(Received 11 June 2010; revised manuscript received 13 January 2011; published 20 September 2011)

We report on K^{*0} production at midrapidity in Au + Au and Cu + Cu collisions at $\sqrt{s_{NN}} = 62.4$ and 200 GeV collected by the Solenoid Tracker at the Relativistic Heavy Ion Collider detector. The K^{*0} is reconstructed via the hadronic decays $K^{*0} \to K^+\pi^-$ and $\overline{K^{*0}} \to K^-\pi^+$. Transverse momentum, p_T, spectra are measured over a range of p_T extending from 0.2 GeV/c up to 5 GeV/c. The center-of-mass energy and system size dependence of the rapidity density, dN/dy, and the average transverse momentum, $\langle p_T \rangle$, are presented. The measured $N(K^{*0})/N(K)$ and $N(\phi)/N(K^{*0})$ ratios favor the dominance of rescattering of decay daughters of K^{*0} over the hadronic regeneration for the K^{*0} production. In the intermediate p_T region ($2.0 < p_T < 4.0$ GeV/c), the elliptic flow parameter, v_2, and the nuclear modification factor, $R_{\rm CP}$, agree with the expectations from the quark coalescence model of particle production.

DOI: 10.1103/PhysRevC.84.034909 PACS number(s): 25.75.Dw, 13.75.Cs

I. INTRODUCTION

The main motivation for studying heavy-ion collisions at high energy is the study of quantum chromodynamics (QCD) in extreme conditions of high temperature and high energy density [1–4]. Ultrarelativistic nucleus-nucleus collisions at the Relativistic Heavy Ion Collider (RHIC) create nuclear matter of high energy density over an extended volume, allowing QCD predictions to be tested in the laboratory. At high temperature and density, QCD predicts a phase transition from nuclear matter to a state of deconfined quarks and gluons known as the quark gluon plasma (QGP). One of the proposed signatures of the QGP state is the modification of vector-meson production rates and their in-medium properties [5–7].

The K^* meson is of particular interest due to its very short lifetime and its strange valence quark content. This makes the K^* meson sensitive to the properties of the dense matter and strangeness production from an early partonic phase [8,9]. Since the lifetime of the K^* is $\sim$4 fm/c, less than the lifetime of the system formed in heavy-ion collisions [10], the K^* is expected to decay, rescatter, and regenerate all the way to the kinetic freeze-out (vanishing elastic collisions). The characteristic properties of the resonance may be modified due to high density and/or high temperature of the medium causing in-medium effects. Various in-medium effects are partonic interaction with the surrounding matter, the interference between different scattering channels, and effects due to rescattering of the decay daughter particles [11,12]. Measurement of the K^* meson properties such as mass, width, and yields at various transverse momenta can provide insight for understanding the dynamics of the medium created in heavy-ion collisions.

Of particular interest in resonance production is understanding the role of rescattering and regeneration effects. Due to the short K^* lifetime, the pions and kaons from the K^* that decay at the chemical freeze-out rescatter with other hadrons. This would then inhibit the reconstruction of the parent K^*. However, in the presence of a large population of pions and kaons, these may scatter into a K^* resonance state and thus contribute to the final measured yield [13]. The interplay of these two competing processes becomes relevant for determining the K^* yield in the hadronic medium. These processes depend on the time interval between chemical (vanishing inelastic collisions) and kinetic freeze-out, the source size, and the interaction cross section of the daughter hadrons. Since the $\pi\pi$ interaction cross section [14] is larger (factor 5) than the πK interaction cross section [15], the final observable K^* yield may decrease compared to the primordial yield. A suppression of the yield ratio such as $N(K^*)/N(K)$ or $N(K^*)/N(\phi)$ is expected in heavy-ion collisions compared to the same in $p + p$ collisions at similar collision energies. This suppression can be used to set a lower limit on the time difference between the chemical and the kinetic freeze-out [9,16]. The experimental data on the system size, beam energy, and centrality dependence of this suppression can be used to correlate the lifetime of the fireball with its size. Although the measured values of the resonance yield, mean p_T, and the elliptic anisotropy coefficient v_2 are all expected to be affected by collisional dissociation processes, semihard scattering, and jet fragmentation, the measurements presented in this paper have been discussed within the framework of rescattering and regeneration.

The nuclear modification factors such as R_{AA} and $R_{\rm CP}$ [17] are of vital importance in differentiating between the effect of hadron mass and hadron type (baryon or meson) in particle production. In the intermediate p_T range ($2.0 < p_T < 4.0$ GeV/c), the $R_{\rm CP}$ of Λ (a baryon) and K^0_S (a meson), as measured by the Solenoid Tracker at the Relativistic Heavy Ion Collider (STAR), differ. The observed differences can be understood as coming from differences in particle type (the baryon-meson effect), in agreement with the quark coalescence model [17,18]. Because the mass of the K^* meson is comparable to the mass of the Λ baryon, it is interesting to compare the $R_{\rm CP}$ of K^* with those of K^0_S and Λ to check whether the results confirm to the expectations of the quark coalescence model. Previous measurements of $R_{\rm CP}$ for K^* in Au + Au collisions at $\sqrt{s_{NN}} = 200$ GeV were not precise enough to make such a conclusion [9]. In this paper we present a measurement of $R_{\rm CP}$ of the K^* from a higher statistics data set collected in the year 2004.

In the intermediate p_T range, the elliptic flow parameter, v_2, for different hadrons shows a deviation from the particle mass ordering as seen in the low-p_T regime ($p_T < 1.5$ GeV/c) [17,19,20]. For identified hadrons, v_2 follows a scaling with the number of constituent quarks, n, as expected from the quark coalescence model [12,17]. The K^* meson is expected to follow the scaling law with $n = 2$. The K^* produced via regeneration of kaons and pions during hadronization, on the other hand, would follow the $n = 4$ scaling [21]. Previous STAR measurements with a smaller data sample found $n = 3 \pm 2$ [9] and could not conclusively determine the K^* production mechanism. The additional v_2 data presented in this paper, for Au + Au collisions at 200 GeV, may conclusively provide information about the K^* production mechanism in the intermediate-p_T range.

In previous STAR measurements, K^* production was studied using data from Au + Au, $p + p$, and d+ Au collisions at 200 GeV [9,22] and Au + Au collisions at 130 GeV [8]. The hadronic decay channels used in these analyses were $K^{*0} \to K^+\pi^-$, $\overline{K^{*0}} \to K^-\pi^+$, and $K^{*\pm} \to K^0_S + \pi^\pm$. In this paper we present new data on the p_T distribution, $\langle p_T \rangle$, and dN/dy of K^{*0} in Au + Au collisions at $\sqrt{s_{NN}} = 62.4$ GeV and Cu + Cu collisions at $\sqrt{s_{NN}} = 62.4$ and 200 GeV. The data sample for Au + Au collisions at 200 GeV is 6.5 times larger than previous measurements, allowing us to make more quantitative conclusions from the v_2 and $R_{\rm CP}$ measurements. This broad systematic study, with two different colliding beam energies and two different colliding species, enables us to study the system size and energy dependence of various K^{*0} properties in heavy-ion collisions. To reduce statistical errors, the samples of K^{*0} and $\overline{K^{*0}}$ were combined and are referred to as K^{*0} in the present work, unless specified otherwise.

The paper is organized as follows. In Sec. II we discuss the detectors used in this analysis and details of the analysis procedure. For more details on the mixed-event procedure used to extract the K^{*0} yields, the systematic uncertainty estimation, and the procedure to obtain v_2, we refer the reader to our earlier publications [8,9]. Our results on p_T spectra, dN/dy, $\langle p_T \rangle$, particle ratios, v_2, and $R_{\rm CP}$ of K^{*0} are presented in Sec. III. The results are summarized in Sec. IV.

TABLE I. List of data sets used in the analysis. Cuts on V_Z, centrality range selected, and number of events used are also given.

Collision systems	Centrality	$\lvert V_Z\rvert$ cm	Events
Au + Au (62.4 GeV)	0–80%	<30	7×10^6
Cu + Cu (62.4 GeV)	0–60%	<30	8×10^6
Au + Au (200 GeV)	0–80%	<30	13×10^6
Cu + Cu (200 GeV)	0–60%	<30	19×10^6

II. EXPERIMENT AND DATA ANALYSIS

The results reported here represent data taken from Au + Au collisions at $\sqrt{s_{NN}} = 62.4$ and 200 GeV in the year 2004 and Cu + Cu collisions at $\sqrt{s_{NN}} = 62.4$ and 200 GeV in the year 2005, using the STAR detector at RHIC [23]. The primary tracking device within STAR, the Time Projection Chamber (TPC) [24], was used for the track reconstruction of the decay daughters of K^{*0}. The TPC provides particle identification and momentum information of the charged particles by measuring their ionization energy loss, dE/dx [24].

The data were collected with a minimum bias (MB) trigger. In Au + Au collisions the MB trigger requires a coincidence between two zero degree calorimeters (ZDC) [25]. The ZDCs are located 18 m away from the nominal collision point (center of TPC), in the beam direction, at polar angle, θ, less than 2 mrad. For Cu + Cu collisions at 62.4 GeV, the minimum bias trigger was a combination of the signals from the ZDC and the Beam Beam Counter (BBC). The BBC at $3.3 < \eta < 5.0$ compensates for the trigger inefficiency of the ZDC in central events. To ensure uniform acceptance in the pseudorapidity, η, range studied, events with primary vertex position, V_Z, within ± 30 cm from the center of the TPC along the beam line were selected.

Centrality is defined as function of the fractional cross section measured as function of the uncorrected charged particle multiplicity within the pseudorapidity window $|\eta| < 0.5$ for all events [9,26]. The most peripheral events were not taken into account due to large trigger and vertex finding inefficiencies. Table I lists all the collision systems studied with the V_Z cut, centrality range, and number of events used in the analysis.

Figure 1 shows the typical dE/dx measured by the TPC in Au + Au collisions at 200 GeV for the year 2004 as a function of momentum, p, divided by charge of the particle, q. The different solid lines in the Fig. 1 represent modified Bethe-Bloch predictions for different particle species [27–29]. More details about the respective purity and contamination of individual particle species is described in Ref. [29]. The $e^{\pm}$ and $K^{\pm}$ dE/dx bands merge beyond p_T of 0.5 GeV/c and the $K^{\pm}$ and $\pi^{\pm}$ dE/dx bands merge beyond p_T of 0.75 GeV/c. In the lower p_T the main source of contamination to π is from misidentification of muons. It is about 4% for $p_T = 0.2$ GeV/c and reduces to less than 1% for $p_T = 1.2$ GeV/c. The main source of contamination for K is from electrons, the level of which varies from 12% to 4% with p_T. The efficiency and acceptance for kaons and pions as a function of transverse momentum is also described.

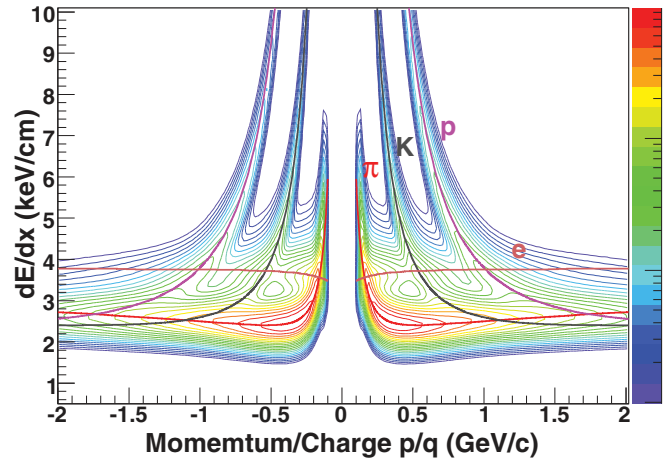

FIG. 1. (Color online) dE/dx for charged particles versus momentum divided by charge of the particle as measured in STAR TPC for Au + Au collisions at $\sqrt{s_{NN}} = 200$ GeV. The curves are the Bethe-Bloch predictions for different particle species.

The charged pions and kaons can be separated in momenta up to about 0.75 GeV/c while (anti-)protons can be separated in momenta up to about 1.1 GeV/c. The particle identification can be quantitatively described by the variable N_σ, which for pions is defined as:

$$N_{\sigma\pi} = \frac{1}{R} \log \frac{(dE/dx)_{\text{measured}}}{\langle dE/dx \rangle_\pi}, \tag{1}$$

where dE/dx_{measured} is the measured energy loss for a track, $\langle dE/dx \rangle_\pi$ is the expected mean energy loss for a pion track at a given momentum [28,29], and R is the dE/dx resolution which is around 8.1%.

K^{*0} mesons were reconstructed from their hadronic decay channels, $K^{*0} \to K^+\pi^-$ and $\overline{K^{*0}} \to K^-\pi^+$, using charged tracks reconstructed with the TPC. Because the K^{*0} decays within a very short time, its daughter particles seem to originate from the interaction point. Charged kaons and pions with a distance of closest approach to the primary vertex (DCA) less than 1.5 cm were considered for Au + Au collisions at 62.4 GeV and Cu + Cu collisions at 62.4 and 200 GeV. In the case of 200 GeV Au + Au collisions, the DCA cut was set at 2.0 cm. The charged pion and kaon primary tracks thus selected were required to have their respective N_σ values less than 2, with at least 15 fit points inside the TPC. This was done to ensure good track fitting with good momentum and dE/dx resolution. Further, the ratio of the number of fit points to the number of maximum possible fit points was required to be greater than 0.55 to avoid selection of split tracks. In Au + Au collisions at 62.4 GeV and Cu + Cu collisions at 62.4 and 200 GeV all the candidate tracks were required to have $|\eta| < 1$ while the tracks for the 200-GeV Au + Au collisions were required to have $|\eta| < 0.8$ to avoid the acceptance drop at the high-η range. All tracks selected were also required to satisfy the condition that their p_T were greater than 0.2 GeV/c. All the cuts used for the K^{*0} analysis are summarized in Table II.

TABLE II. List of track cuts for charged kaons and charged pions used in the K^{*0} analysis in Au + Au and Cu + Cu collisions at 62.4 and 200 GeV. NFitPnts is the number of fit points of a track in the TPC. MaxPnts is the number of maximum possible points of the track in the TPC.

Cut	Values
$N_{\sigma K}$	$(-2.0, +2.0)$
$N_{\sigma \pi}$	$(-2.0, +2.0)$
Kaon p_T (GeV/c)	(0.2, 10.0)
Pion p_T (GeV/c)	(0.2, 10.0)
NFitPnts	>15
NFitPnts/Max Pnts	>0.55
Kaon and pion η	$\lvert\eta\rvert < 1.0$
	$\lvert\eta\rvert < 0.8$ (Au + Au 200 GeV)
DCA	<1.5 cm
	<2.0 cm (Au + Au 200 GeV)
Pair rapidity (y)	$\lvert y\rvert < 0.5$

In a typical event, several hundred tracks originate from the primary collision vertex. It is impossible to distinguish the tracks corresponding to the decay daughters of the K^{*0} from other primary tracks. The K^{*0} was reconstructed by calculating the invariant mass for each unlike-sign $K\pi$ pair in an event. The resultant distribution consists of the true K^{*0} signal and contributions arising from random combination of unlike-sign $K\pi$ pairs. The true K^{*0} signal constitutes a very small fraction of the total invariant mass spectrum. The large random combinatorial background must be subtracted from the unlike-sign $K\pi$ invariant mass distribution to extract the K^{*0} yield. This random combinatorial background distribution is obtained using the mixed-event technique [22,26,30,31]. In the mixed-event technique, the reference background distribution was built with uncorrelated unlike-sign $K\pi$ pairs from different events. For generating the mixed events, the data sample was divided into 10 bins in event multiplicity and 10 bins in V_Z. Unlike-sign $K\pi$ pairs from events having similar event multiplicity and V_Z were selected for mixing. This was done to ensure that the characteristics of the mixed events generated were similar to the actual data. The generated mixed-event sample was properly normalized to subtract the background from the same event unlike-sign invariant mass spectrum. The normalization factor was calculated by taking the ratio between the number of entries in the unlike-sign and the mixed-event distributions with invariant mass greater than 1.2 GeV/c^2. The $K\pi$ pairs are less likely to be correlated in this region. The typical value of the normalization factor for

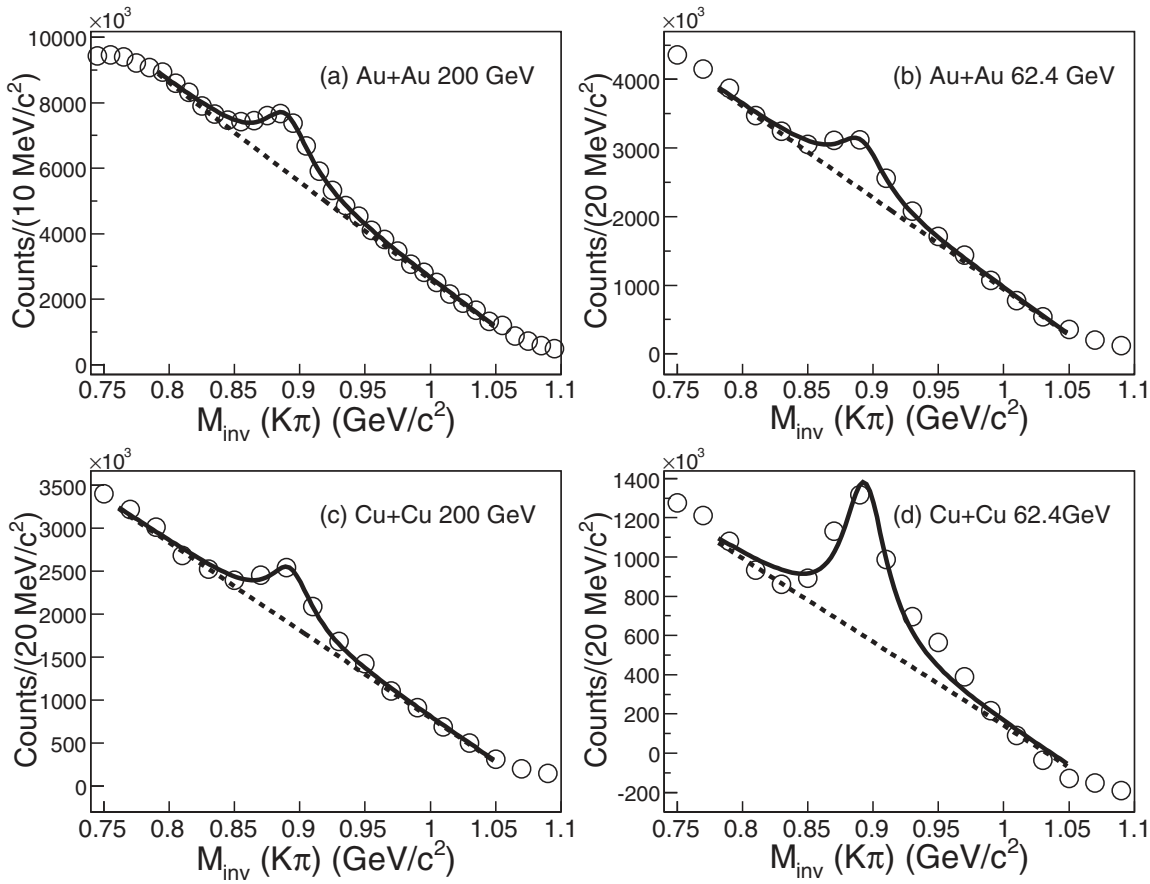

FIG. 2. The $K\pi$ pair invariant mass distribution integrated over the K^{*0} p_T for minimum bias Au + Au and Cu + Cu collisions at $\sqrt{s_{NN}} = 62.4$ and 200 GeV after the mixed-event background subtraction. The solid curve is the signal fit to a Breit-Wigner function Eq. (2) plus linear function Eq. (3) while the dashed line is the linear function representing the residual background. The statitical errors are small and are within the symbol size.

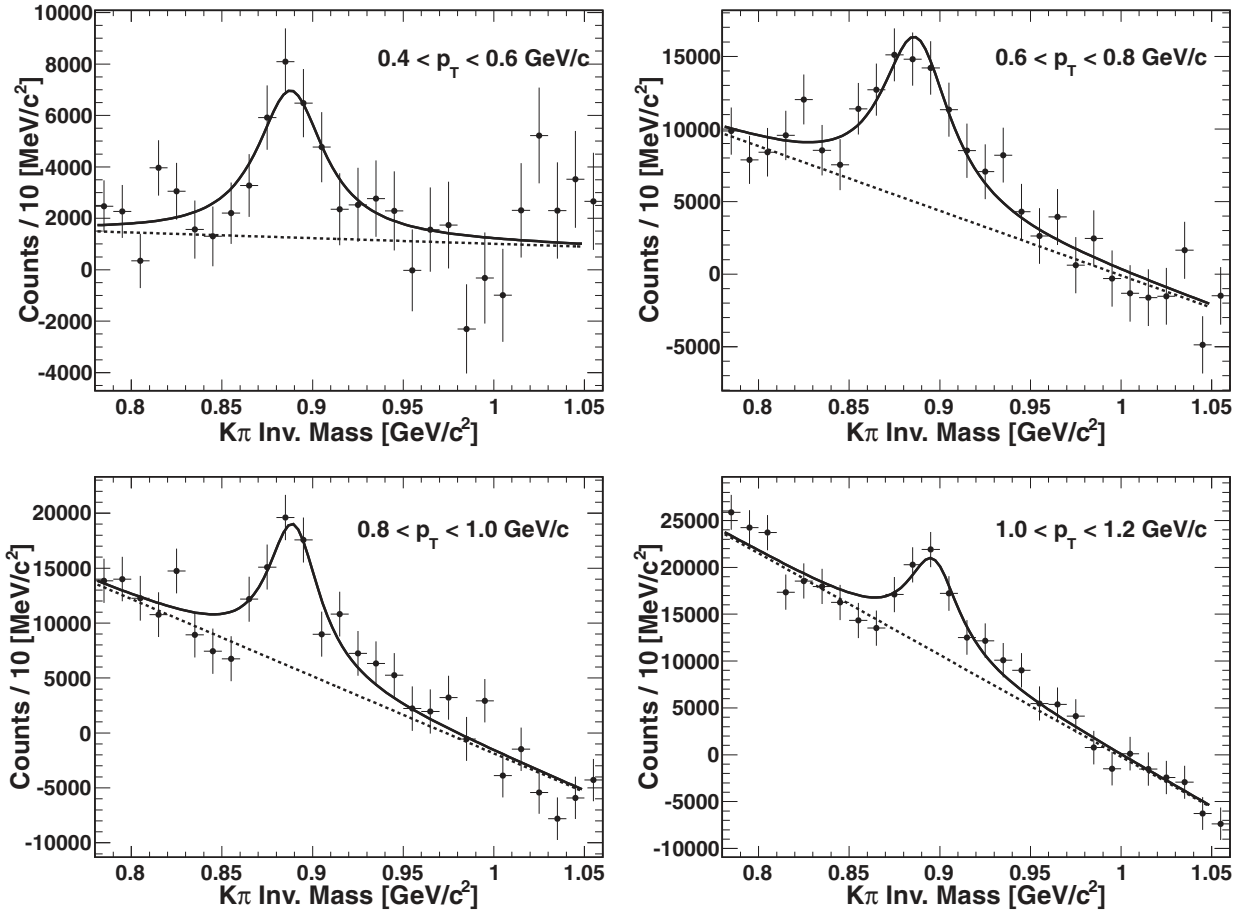

FIG. 3. The $K\pi$ pair invariant mass distribution for various p_T bins [(top left) $p_T = 0.4$–0.6 GeV/c; (top right) $p_T = 0.6$–0.8 GeV/c; (bottom left) $p_T = 0.8$–1.0 GeV/c; and (bottom right) $p_T = 1.0$–1.2 GeV/c] in Au + Au collisions at $\sqrt{s_{NN}} = 62.4$ GeV after the mixed-event background subtraction. The solid curve is the signal fit to a Breit-Wigner function Eq. (2) plus linear function Eq. (3) while the dashed line is the linear function representing the residual background. The errors shown are statistical.

most p_T bins vary between 0.1284 to 0.1285 for Au + Au collisions at $\sqrt{s_{NN}} = 62.4$ GeV.

Figure 2 shows the background-subtracted and p_T-integrated unlike-sign $K\pi$ invariant mass spectra corresponding to minimum bias Au + Au and Cu + Cu collisions at $\sqrt{s_{NN}} = 62.4$ and 200 GeV. Figure 3 shows typical the background-subtracted unlike-sign $K\pi$ invariant mass spectra corresponding to minimum bias Au + Au at $\sqrt{s_{NN}} =$ 62.4 GeV for four p_T bins of 0.4–0.6, 0.6–0.8, 0.8–1.0, and 1.0–1.2 GeV/c. The uncertainty due to different mixed-event normalization factors as a function of p_T was estimated and included in systematic error. The signal-to-background ratio as a function of the $K\pi$ pair p_T for Au + Au collisions at $\sqrt{s_{NN}} =$ 200 GeV is shown in Fig. 4. The values are of similar order for other collision systems. The signal-to-background ratio, S/B, is observed to increase with decreasing multiplicity of the events and shows an increase with increasing p_T. In the unlike-sign spectrum we also could have higher and/or lower $K\pi$ mass resonant states and nonresonant correlations due to particle misidentification and effects from elliptic flow in noncentral collisions. These effects contribute significantly to the residual correlations near the signal [9] that are not present in the mixed-event sample. These residual correlations are also subtracted from the background using a background function described in Sec. III.

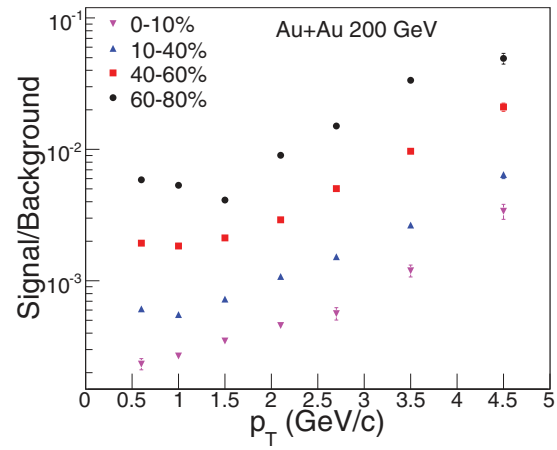

FIG. 4. (Color online) The signal-to-background ratio for K^{*0} measurements as a function of p_T for different collision centrality bins in Au + Au collisions at 200 GeV.

III. RESULTS

A. $M_{K\pi}$ peak and width

The invariant mass distributions (typical distributions shown in Fig. 2) for various p_T bins in Au + Au and Cu + Cu collisions at $\sqrt{s_{NN}} = 62.4$ and 200 GeV were fit using a function representing a nonrelativistic Breit-Wigner (BW) shape plus a linear residual background (RBG). The BW and the RBG parts are as given below.

$$\mathrm{BW} = \frac{\Gamma_0}{(M_{K\pi} - M_0)^2 + \frac{\Gamma_0^2}{4}}, \tag{2}$$

$$\mathrm{RBG} = a + bM_{K\pi}, \tag{3}$$

In the above equations, M_0 and Γ_0 are the mass and width of the K^{*0}; a and b are the intercept and slope for the linear residual background.

The variations of M_0 and Γ_0 with p_T are shown in Fig. 5. The error bars shown correspond to statistical uncertainties while the bands represent systematic uncertainties. In the low-p_T region (<1 GeV/c), the measured widths are consistent with the Particle Data Group (PDG) value of 50.3 MeV/c^2 while the measured masses are within 2σ of the PDG value of 896.0 MeV/c^2 [27]. In the higher-p_T range (>1 GeV/c), both the mass and width of K^{*0} are seen to be consistent with the PDG values. We observe no significant dependence of K^{*0} mass and width on beam energy and colliding ion species studied. The systematic uncertainties on the K^{*0} mass and width measurement were evaluated bin by bin, as a function of p_T: (i) an uncertainty on the signal fit was evaluated by replacing the nonrelativistic BW function with a relativistic BW function, (ii) an uncertainty on the background was evaluated by varying residual background functions by using higher-order polynomials, and (iii) an uncertainty on track selection was calculated by varying the particle identification criteria and different cuts on the daughter tracks. In the above analysis, low-p_T kaon tracks were corrected for energy loss due to multiple scattering in the detector [26,29].

B. Transverse momentum spectra

The K^{*0} invariant yields as a function of p_T were evaluated by correcting the extracted raw yields for detector acceptance and reconstruction efficiency. The raw yield was obtained by fitting the data to the BW + RBG function. The efficiency multiplied by acceptance was obtained by embedding Monte Carlo (MC) simulations of kaons and pions from K^{*0} decays into the real data using STAR GEANT and passing these embedding data through the same reconstruction chain as for the real data [32]. In addition, the yields were corrected for collision vertex finding efficiency and the decay branching ratio of 0.66. The vertex finding efficiency is 94.5% for Au + Au collisions at 62.4 GeV and 92.2% for Cu + Cu collisions at 62.4 and 200 GeV. The vertex finding efficiency for Au + Au collisions at 200 GeV is 100%. The variation of efficiency multiplied by acceptance with p_T, for various centralities in the Au + Au and Cu + Cu system for $\sqrt{s_{NN}} = 200$ GeV, is depicted in Fig. 6. The absence of centrality dependence

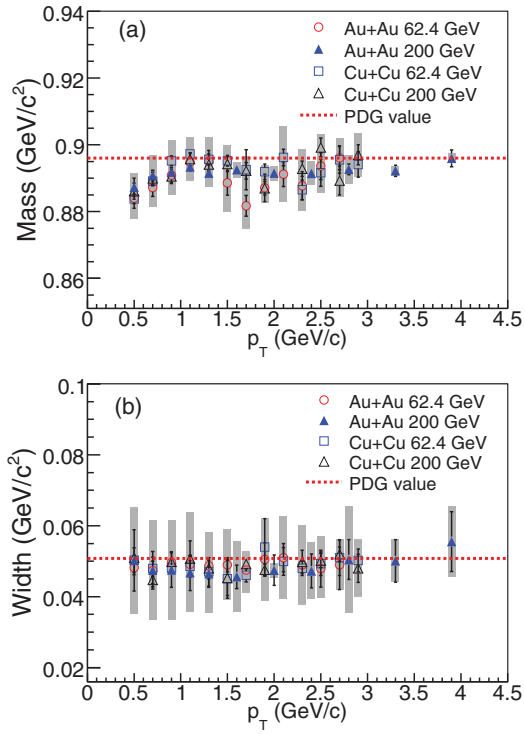

FIG. 5. (Color online) K^{*0} (a) mass and (b) width as a function of p_T for minimum bias Au + Au and Cu + Cu collisions at $\sqrt{s_{NN}} =$ 62.4 and 200 GeV. The dashed line represents the PDG values of 896.0 MeV/c^2 and 50.3 MeV/c^2 for mass and width, respectively.

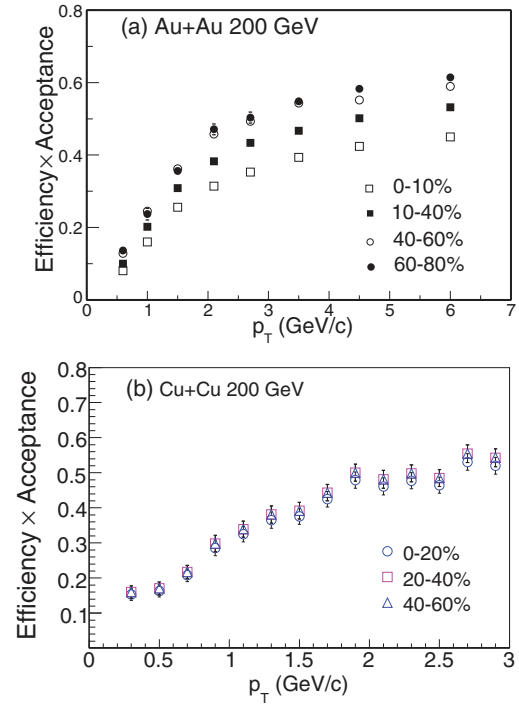

FIG. 6. (Color online) The K^{*0} reconstruction efficiency multiplied by the detector acceptance as a function of p_T in (a) Au + Au ($|\eta| < 0.8$) and (b) Cu + Cu ($|\eta| < 1.0$) collisions at 200 GeV for different collision centrality bins.

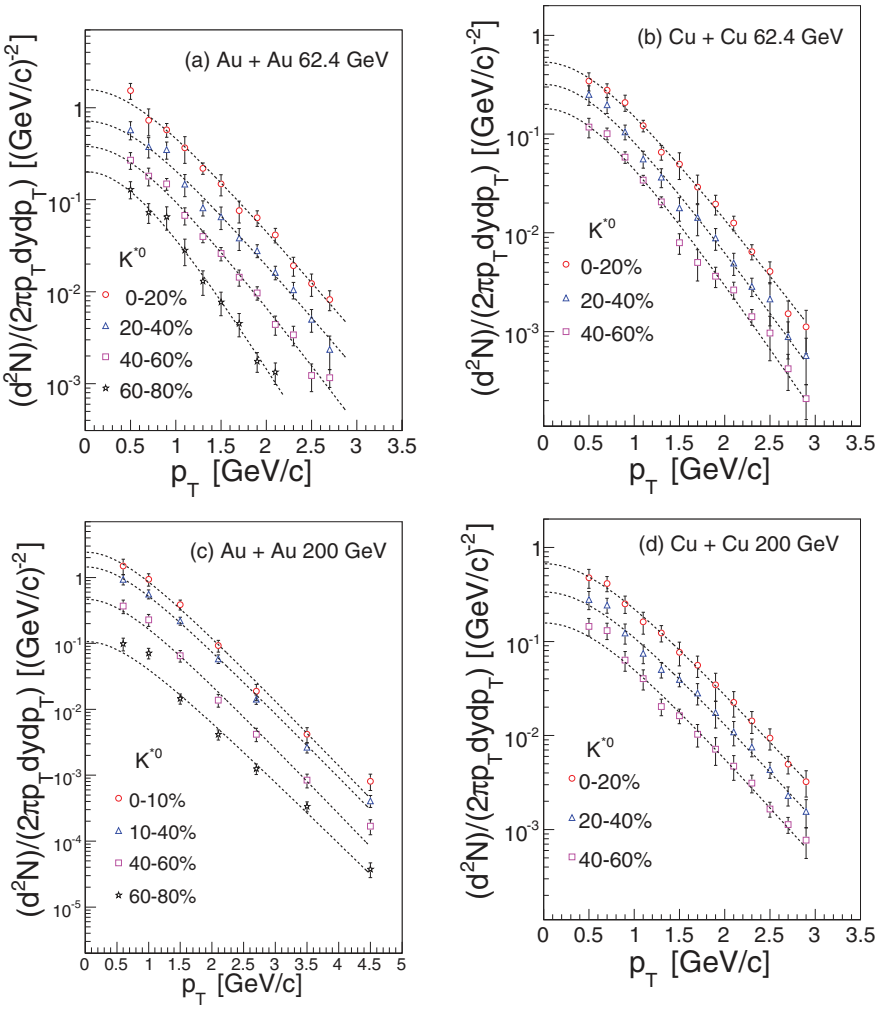

FIG. 7. (Color online) Midrapidity K^{*0} p_T spectra for various collision centrality bins in Au + Au and Cu + Cu collisions at $\sqrt{s_{NN}} = 62.4$ and 200 GeV. The dashed lines represent the exponential fit to data. The errors shown are quadratic sums of statistical and systematic uncertainties.

in the efficiency multiplied by acceptance for the Cu + Cu system is due to small variation in total multiplicity across the collision centrality studied compared to those for the Au + Au system.

Figure 7 shows the p_T spectra of K^{*0} at midrapidity ($|y| < 0.5$) in Au + Au and Cu + Cu collisions at $\sqrt{s_{NN}} = 62.4$ and 200 GeV for different collision centralities. The dashed lines are the exponential fits to the K^{*0} data. The fitting exponential function is defined as

$$\frac{1}{2\pi m_T}\frac{d^2N}{dydm_T} = \frac{dN/dy}{2\pi T(M_0+T)}e^{-(m_T-M_0)/T}, \qquad (4)$$

where the inverse slope parameter T and yield dN/dy are free parameters. M_0 is the mass of the K^{*0}. The above function is found to provide good fits to the data for both collision systems. The $\langle p_T \rangle$, obtained using the above functional form for the p_T distributions, are presented in the following section together with the midrapidity yields dN/dy.

C. dN/dy and $\langle p_T \rangle$

The K^{*0} dN/dy yield at midrapidity plotted as a function of average number of participating nucleons, $\langle N_{\rm part} \rangle$, is shown in Fig. 8. The dN/dy for K^{*0} presented here was calculated by using the data points in the measured range of the p_T spectrum while assuming an exponential behavior outside the fiducial range. The K^{*0} integrated yield is higher for center-of-mass energies of 200 GeV than 62.4 GeV. For collisions at a given beam energy with similar $\langle N_{\rm part} \rangle$, the dN/dy is similar for Au + Au and Cu + Cu systems. A similar behavior was observed for ϕ mesons at RHIC [26].

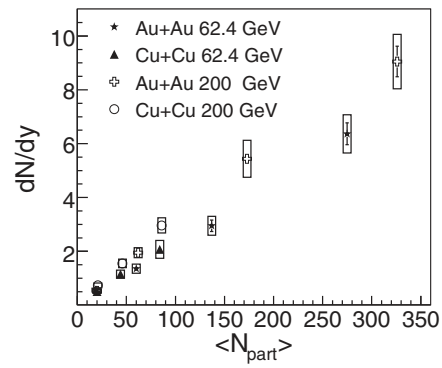

FIG. 8. The midrapidity yields dN/dy of K^{*0} as a function of the average number of participating nucleons, $\langle N_{\rm part} \rangle$, for Au + Au and Cu + Cu collisions at $\sqrt{s_{NN}} = 62.4$ and 200 GeV. The boxes represent the systematic uncertainties.

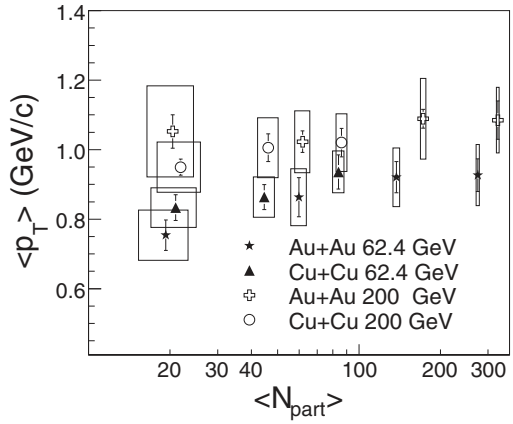

FIG. 9. The midrapidity K^{*0} $\langle p_T \rangle$ as a function $\langle N_{\rm part} \rangle$ for Au + Au and Cu + Cu collisions at $\sqrt{s_{NN}} = 62.4$ and 200 GeV. The boxes represent the systematic uncertainties.

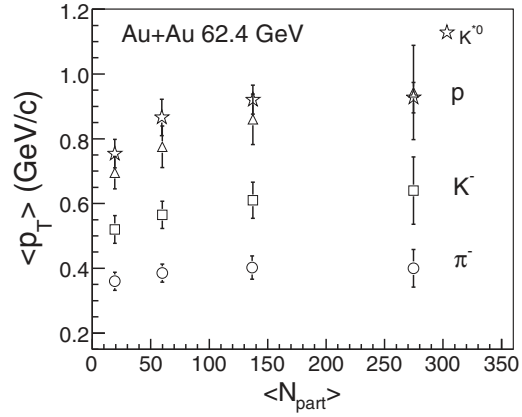

FIG. 10. The midrapidity $\langle p_T \rangle$ of π, K, p, and K^{*0} as a function of $\langle N_{\rm part} \rangle$ for Au + Au collisions at $\sqrt{s_{NN}} = 62.4$ GeV.

The K^{*0} $\langle p_T \rangle$ at midrapidity plotted as a function of $\langle N_{\rm part} \rangle$, is shown in Fig. 9 for Au + Au and Cu + Cu collisions at $\sqrt{s_{NN}} = 62.4$ and 200 GeV. The $\langle p_T \rangle$ for K^{*0} presented here was calculated by using the data points in the measured range of the p_T spectrum while assuming an exponential behavior outside the fiducial range. No significant centrality and colliding ion size dependence could be observed. However, the $\langle p_T \rangle$ values for collisions at 200 GeV are seen to be slightly higher than those from 62.4 GeV in both Au + Au and Cu + Cu collisions. Previous measurements of $\langle p_T \rangle$ of K^{*0} in heavy-ion collisions have been shown to be higher than the corresponding values in $p + p$ collisions [9]. This may be understood from the following. According to ultrarelativistic quantum molecular dynamics transport model calculations [33], K^{*0}s are more likely to be reconstructable in the high-p_T region than in the low-p_T region. This is because high-p_T K^{*0}s are more likely to escape the medium before the kinetic freeze-out stage (if their daughter particles suffer less rescattering in the medium) and are thus less affected by in-medium effects [34,35]. This would result in a higher value of the $\langle p_T \rangle$. In case of elementary p+p collisions low p_T resonances can also get efficiently detected (due to much reduced rescattering/in-medium effects) along with the ones with higher p_T. This makes the p_T spectrum steeper. Therefore $\langle p_T \rangle$ has a lower value when compared with heavy ions.

Figure 10 shows the $\langle p_T \rangle$ of different particle species (π, K, p, and K^{*0}) in Au + Au collision at $\sqrt{s_{NN}} = 62.4$ GeV as a function of $\langle N_{\rm part} \rangle$. The $\langle p_T \rangle$ of K^{*0} is higher than the $\langle p_T \rangle$ of kaons and pions and closer to that of protons. This indicates that the $\langle p_T \rangle$ is strongly coupled with the mass of the particle, in agreement with similar observations made previously in Au + Au and d + Au collisions at 200 GeV [9,22]. Table III lists the dN/dy and $\langle p_T \rangle$ of K^{*0} for various collision systems at different collision centralities and beam energies studied.

The systematic uncertainties on K^{*0} dN/dy and $\langle p_T \rangle$ were estimated as follows [35]: (a) an uncertainty on the K^{*0} signal fit of the invariant mass spectrum was evaluated by

TABLE III. The K^{*0} dN/dy and $\langle p_T \rangle$ at $|y| < 0.5$ measured in Au + Au and Cu + Cu collisions at 62.4 and 200 GeV for different collision centralities. Both statistical and systematic uncertainties are given. The error given for T is statistical only.

Collision systems	Centrality	$\langle N_{\rm part} \rangle$	dN/dy	T (GeV)	$\langle p_T \rangle$ (GeV)
Au + Au (62.4 GeV)	0–20%	275	$6.4 \pm 0.4 \pm 0.7$	0.36 ± 0.02	$0.93 \pm 0.05 \pm 0.09$
	20–40%	137	$2.9 \pm 0.2 \pm 0.4$	0.35 ± 0.02	$0.92 \pm 0.05 \pm 0.08$
	40–60%	60	$1.4 \pm 0.1 \pm 0.2$	0.32 ± 0.01	$0.86 \pm 0.06 \pm 0.08$
	60–80%	19	$0.56 \pm 0.03 \pm 0.07$	0.26 ± 0.02	$0.75 \pm 0.04 \pm 0.07$
Cu + Cu (62.4 GeV)	0–20%	84	$2.07 \pm 0.07 \pm 0.30$	0.35 ± 0.01	$0.94 \pm 0.05 \pm 0.06$
	20–40%	44	$1.15 \pm 0.06 \pm 0.20$	0.33 ± 0.01	$0.86 \pm 0.04 \pm 0.06$
	40–60%	20	$0.51 \pm 0.03 \pm 0.07$	0.31 ± 0.01	$0.83 \pm 0.04 \pm 0.06$
Au + Au (200 GeV)	0–10%	326	$9.05 \pm 0.57 \pm 1.01$	0.41 ± 0.02	$1.09 \pm 0.06 \pm 0.094$
	10–40%	173	$5.43 \pm 0.17 \pm 0.69$	0.43 ± 0.02	$1.09 \pm 0.03 \pm 0.12$
	40–60%	62	$1.95 \pm 0.07 \pm 0.18$	0.39 ± 0.02	$1.02 \pm 0.03 \pm 0.09$
	60–80%	20	$0.53 \pm 0.03 \pm 0.08$	0.40 ± 0.03	$1.05 \pm 0.05 \pm 0.13$
Cu + Cu (200 GeV)	0–20%	86	$2.96 \pm 0.12 \pm 0.30$	0.40 ± 0.01	$1.0 \pm 0.04 \pm 0.08$
	20–40%	46	$1.55 \pm 0.06 \pm 0.20$	0.40 ± 0.02	$1.0 \pm 0.04 \pm 0.09$
	40–60%	21	$0.73 \pm 0.03 \pm 0.09$	0.40 ± 0.02	$0.95 \pm 0.02 \pm 0.07$
$p + p$ (200 GeV)		2	$0.005 \pm 0.002 \pm 0.006$	0.20 ± 0.01	$0.81 \pm 0.02 \pm 0.14$

TABLE IV. The contributions for various sources for estimating the total systematic uncertainties for K^{*0} at midrapidity ($|y| < 0.5$) on dN/dy and $\langle p_T \rangle$ in 0–20% Au + Au collisions at 62.4 GeV. The systematic uncertainties are similar for other collision systems.

Different sources	dN/dy	$\langle p_T \rangle$ (GeV/c)
Exponential fit	0%	0%
Levy fit	5.24%	0.44%
Background function (higher-order polynomial)	4.49%	2.88%
Relativistic Breit-Wigner	2.64%	0.542%
$\lvert V_Z \rvert < 20$ cm	1.6%	1.05%
Track type (K^{*0})	3.6%	4.3%
Track type ($\overline{K}^{*0}$)	4.05%	5.96%
NFitPnts = 22	4.32%	1.35%
$\lvert N_{\sigma\pi}, N_{\sigma K} \rvert < 3$	4.45%	4.87%
Total sys. uncertainty	11.18%	9.47%

replacing the nonrelativistic BW function with a relativistic BW function, (b) an uncertainty on the background distribution fit was evaluated by using a higher-order polynomial function, (c) by varying the track types (K^{*0} and $\overline{K}^{*0}$), (d) using different functions such as a Levy function [36,37] to fit the spectra, (e) an uncertainty on track selection was estimated by varying the track cuts such as N_σ cut, NFitPnts cut, and (f) by varying the V_Z cut from 30 to 20 cm. The systematic uncertainties coming from the different sources are listed in Table IV for Au + Au collisions at 62.4 GeV.

D. Particle ratio

Figure 11(a) shows the ratio of K^{*0} and K^- yields, $N(K^{*0})/N(K^-)$, as a function of $\langle N_{\rm part} \rangle$ in Au + Au and Cu + Cu collisions at $\sqrt{s_{NN}} = 62.4$ and 200 GeV. The lines connecting the nucleus-nucleus collision data points are for guide to eye. From the figure, for the nucleus-nucleus collisions no clear beam energy or system size dependence is observed. However, the $p + p$ collision $N(K^{*0})/N(K^-)$ results at respective beam energies are higher than the corresponding values for central nucleus-nucleus collision. The Fig. 11(b) shows the K^{*0}/K^- ratio in Au + Au, Cu + Cu, and d + Au collisions normalized by their corresponding values measured in $p + p$ collisions at $\sqrt{s_{NN}} = 200$ GeV. This $N(K^{*0})/N(K^-)$ double ratio is seen to be much smaller than unity in central Au + Au collisions. In contrast the $N(K^{*0})/N(K^-)$ double ratio is close to unity for d + Au collisions. This suggests possible rescattering of decay daughters of K^{*0} meson, resulting in the loss of reconstructed K^{*0} signal. The rescattering of K^{*0} daughter particles depends on $\sigma_{\pi\pi}$ which is considerably larger than $\sigma_{\pi K}$, but $\sigma_{\pi K}$ is responsible for regeneration of the K^{*0} meson. Therefore, we expect a decrease of the $N(K^{*0})/N(K^-)$ yield ratio in heavy-ion collisions due to possible rescattering of K^{*0} daughter particles. The observed decrease in the K^{*0}/K^- double ratio indicates an extended lifetime for the hadronic phase as we move from $p + p$ and d + Au to Au + Au collisions. The extended lifetime enhances the rescattering effect. Figure 11(c) shows the energy dependence of the $N(K^{*0})/N(K^-)$ ratio for minimum bias Au + Au and Cu + Cu collisions at $\sqrt{s_{NN}} = 62.4$ and 200 GeV. Also included in the figure are values obtained from $p + p$ collisions at 63 GeV [38] and 200 GeV [9]. At both energies, the $N(K^{*0})/N(K^-)$ for $p + p$ collisions is higher than the values in the heavy-ion collisions. This may be attributed to larger rescattering of K^{*0} daughter particles in heavy-ion collisions.

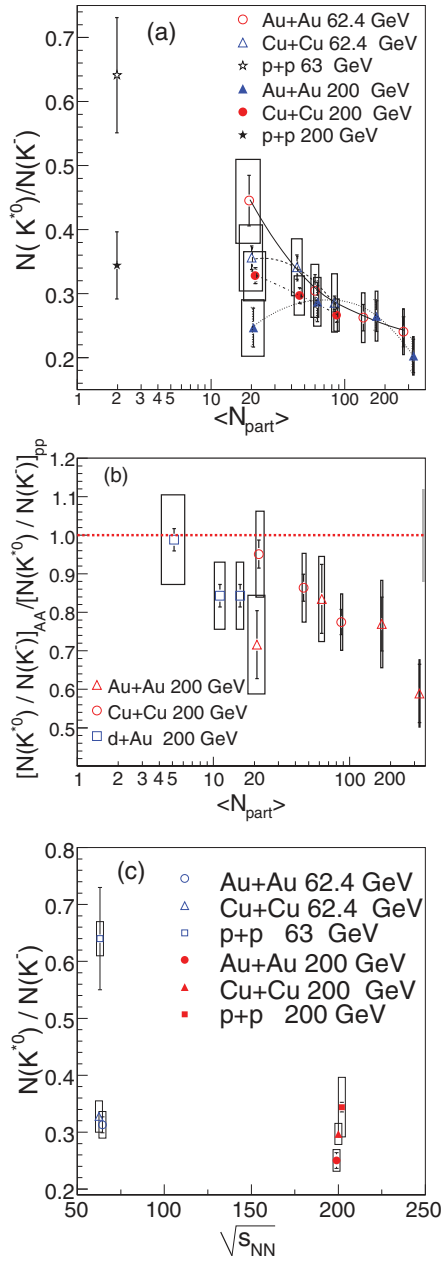

FIG. 11. (Color online) (a) Midrapidity $N(K^{*0})/N(K^-)$ ratio for Au + Au, Cu + Cu, and $p + p$ collisions at $\sqrt{s_{NN}} = 62.4$ and 200 GeV versus $\langle N_{\rm part} \rangle$. (b) Midrapidity $N(K^{*0})/N(K^-)$ in Au + Au, Cu + Cu, and d + Au collisions divided by $N(K^{*0})/N(K^-)$ ratio in $p + p$ collisions at $\sqrt{s_{NN}} = 200$ GeV as a function of $\langle N_{\rm part} \rangle$. (c) Midrapidity $N(K^{*0})/N(K^-)$ ratio in minimum bias Au + Au, Cu + Cu, $p + p$ collisions as a function of $\sqrt{s_{NN}}$. The boxes represents systematic uncertainties. The value of $N(K^{*0})/N(K^-)$ ratio in $p + p$ at 63 GeV is from ISR [38].

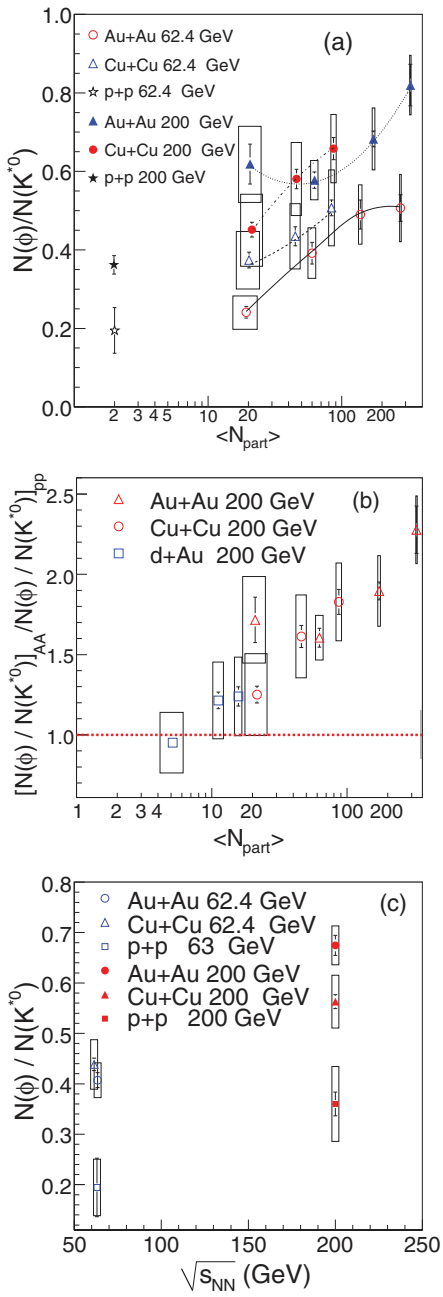

FIG. 12. (Color online) (a) Midrapidity $N(\phi)/N(K^{*0})$ ratio for Au + Au, Cu + Cu, and $p + p$ collisions at $\sqrt{s_{NN}} = 62.4$ and 200 GeV versus $\langle N_{\rm part}\rangle$. (b) Midrapidity $N(\phi)/N(K^{*0})$ in Au + Au, Cu + Cu, and d + Au collisions divided by $N(\phi)/N(K^{*0})$ ratio in $p + p$ collisions at $\sqrt{s_{NN}} = 200$ GeV as a function of $\langle N_{\rm part}\rangle$. (c) Midrapidity $N(\phi)/N(K^{*0})$ ratio in minimum bias Au + Au, Cu + Cu, and $p + p$ collisions as a function of $\sqrt{s_{NN}}$. The boxes represents systematic uncertainties. The values of $N(\phi)/N(K^{*0})$ ratio in $p + p$ at 63 GeV is from ISR [38].

Another ratio of considerable interest is the $N(\phi)/N(K^{*0})$ ratio as both the ϕ and K^{*0} have the same spin and similar mass but different strangeness and lifetime. The lifetime of the ϕ meson is 40 fm/c (~10 times that of K^{*0}). Due to the relatively longer lifetime of the ϕ meson and negligible σ_{KK} [26], we expect both the rescattering and regeneration effects to be negligible for the ϕ meson. Since ϕ has two strange quarks and K^{*0} has one, $N(\phi)/N(K^{*0})$ can also give information regarding strangeness enhancement.

Figure 12(a) depicts the $N(\phi)/N(K^{*0})$ ratio as a function of $\langle N_{\rm part}\rangle$, corresponding to Au + Au and Cu + Cu collisions at $\sqrt{s_{NN}} = 62.4$ and 200 GeV. The lines connecting the nucleus-nucleus collision data points are for guide to eye. We observe that the ratio tends to increase with increasing $\langle N_{\rm part}\rangle$ at a given beam energy. The $N(\phi)/N(K^{*0})$ ratio is higher for $\sqrt{s_{NN}} = 200$ GeV compared to $\sqrt{s_{NN}} = 62.4$ GeV for the various collision centralities. At a given beam energy and $\langle N_{\rm part}\rangle$ the $N(\phi)/N(K^{*0})$ ratio is similar for Au + Au and Cu + Cu collisions and higher than those from $p + p$ collisions. Figure 12(b) also shows $N(\phi)/N(K^{*0})$ ratio in Au + Au, Cu + Cu, and d + Au collisions normalized by their corresponding values measured in $p + p$ collisions at $\sqrt{s_{NN}} = 200$ GeV. We observe that this double ratio increases with collision centrality. The observed increase can also have contributions from strangeness enhancement in more central collisions [26]. It is also important to see the dependence of the ϕ/K ratio to make a remark on strangeness enhancement. The ϕ/K ratio is independent of the centality, colisions species, and beam energy [39]. These observations are supportive of possible dominance of rescattering of daughter particles.

Figure 12(c) shows the energy dependence of the $N(\phi)/N(K^{*0})$ ratio for minimum bias Au + Au and Cu + Cu collisions at $\sqrt{s_{NN}} = 62.4$ and 200 GeV and its values from $p + p$ collisions. The $\sqrt{s} = 63$ GeV value for $p + p$ collisions is from ISR measurements [38]. At both the energies the $N(\phi)/N(K^{*0})$ ratios for $p + p$ collisions are lower than the corresponding values in Au + Au collisions. Furthermore, there is an indication of an increase of the value with beam energy. The study of both ratios $N(K^{*0})/N(K^{-})$ and $N(\phi)/N(K^{*0})$, as a function of colliding species, collision centrality, and beam energy, favors the rescattering scenario over K^{*0} regeneration. The values of the ratios along with the associated uncertainties are shown in Table V.

E. Elliptic flow

We apply the standard reaction plane method as employed in Refs. [40,41] for the analysis of elliptic flow. Here, for a given p_T window, the second-order reaction plane angle, ψ_2, was determined event by event. We have different event planes for every K^{*0} candidate, because for every K^{*0} candidate, its daughter particles are excluded from the event-plane determination. This was later subtracted from the azimuthal angle ϕ of each track in the same event to generate an event plane subtracted azimuthal distribution in the variable $\Phi = (\phi - \psi_2)$. The corresponding distribution, $d^2N/dp_T d\Phi$, in the azimuthal angle Φ for all the events in a given p_T bin were then fitted with a function $A[1 + 2v_2^{\rm obs}\cos(2\Phi)]$, where A is a constant. The fitted value of $v_2^{\rm obs}$ was then divided by the reaction plane resolution factor to obtain v_2 for the p_T window considered [41].

Figure 13 shows v_2 of K^{*0} as a function of p_T in minimum bias Au + Au collisions at $\sqrt{s_{NN}} = 200$ GeV. We fit the data

TABLE V. The midrapidity $N(K^{*0})/N(K^-)$ and $N(\phi)/N(K^{*0})$ yield ratio in Au + Au and Cu + Cu collisions at $\sqrt{s_{NN}} = 62.4$ GeV and 200 GeV for different centralities. The first uncertainty is statistical and the second one is systematic.

Collision systems	Centrality	$N(K^{*0})/N(K^-)$	$N(\phi)/N(K^{*0})$
Au + Au (62.4 GeV)	0–20%	$0.24 \pm 0.02 \pm 0.04$	$0.51 \pm 0.03 \pm 0.09$
	20–40%	$0.26 \pm 0.02 \pm 0.04$	$0.49 \pm 0.03 \pm 0.08$
	40–60%	$0.30 \pm 0.03 \pm 0.04$	$0.39 \pm 0.03 \pm 0.06$
	60–80%	$0.44 \pm 0.04 \pm 0.07$	$0.24 \pm 0.02 \pm 0.04$
Cu + Cu (62.4 GeV)	0–20%	$0.29 \pm 0.01 \pm 0.05$	$0.51 \pm 0.02 \pm 0.1$
	20–40%	$0.34 \pm 0.02 \pm 0.04$	$0.43 \pm 0.02 \pm 0.08$
	40–60%	$0.36 \pm 0.02 \pm 0.05$	$0.37 \pm 0.02 \pm 0.07$
Au + Au (200 GeV)	0–10%	$0.20 \pm 0.03 \pm 0.03$	$0.82 \pm 0.05 \pm 0.08$
	10–40%	$0.26 \pm 0.02 \pm 0.04$	$0.68 \pm 0.02 \pm 0.08$
	40–60%	$0.29 \pm 0.03 \pm 0.04$	$0.58 \pm 0.02 \pm 0.05$
	60–80%	$0.25 \pm 0.03 \pm 0.04$	$0.62 \pm 0.05 \pm 0.1$
Cu + Cu (200 GeV)	0–20%	$0.27 \pm 0.01 \pm 0.03$	$0.66 \pm 0.03 \pm 0.09$
	20–40%	$0.30 \pm 0.01 \pm 0.03$	$0.58 \pm 0.02 \pm 0.09$
	40–60%	$0.33 \pm 0.01 \pm 0.04$	$0.45 \pm 0.02 \pm 0.09$
$p + p$ (200 GeV)	MB	$0.34 \pm 0.01 \pm 0.05$	$0.36 \pm 0.02 \pm 0.07$
$p + p$ (63 GeV, ISR)	MB	$0.64 \pm 0.09 \pm 0.03$	$0.19 \pm 0.06 \pm 0.06$

using the function

$$v_2(p_T, n) = \frac{an}{1 + \exp[-(p_T/n - b)/c]} - dn, \qquad (5)$$

where a, b, c, and d are the parameters extracted from such a fit to v_2 data obtained earlier for K^0_S and Λ [42]. Here n, the number of constituent quarks, is the only free parameter. The best fit of the K^{*0} data with the function as given in Eq. (5) yields a value of $n = 2.0 \pm 0.4$ (χ^2/ndf = 2/6). A similar fit of the combined results of Run II and Run IV data, taken in the years 2002 and 2004, respectively, also yields an identical value of $n = 2.0 \pm 0.4$ (χ^2/ndf = 4/10). This indicates that K^{*0} are dominantly produced from direct quark combinations, and the regenerated K^{*0} component in the hadronic stage is negligible compared to the primordial K^{*0}.

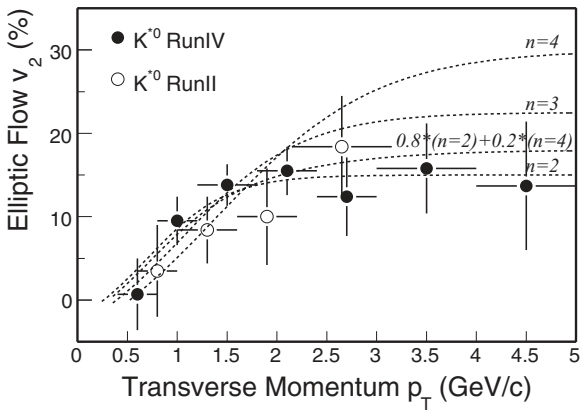

FIG. 13. The K^{*0} v_2 as a function of p_T in minimum bias Au + Au collisions at $\sqrt{s_{NN}} = 200$ GeV. Only statistical uncertainties are shown. The dashed lines represent the v_2 of hadrons with different number of constituent quarks.

F. Nuclear modification factor

Through a measurement of the nuclear modification factors $R_{\rm CP}$ and R_{AA}, one probes the dynamics of particle production during hadronization and in-medium effects [18,37]. The nuclear modification factor $R_{\rm CP}$, which is the ratio of the invariant yields for central to peripheral collisions, normalized by number of binary collisions, $N_{\rm bin}$, is defined as

$$R_{\rm CP} = \frac{[dN/(N_{\rm bin}dp_T)]^{\rm central}}{[dN/(N_{\rm bin}dp_T)]^{\rm peripheral}}, \qquad (6)$$

where $N_{\rm bin}$ is calculated from the Glauber model [29]. We expect $R_{\rm CP}$ to be unity at high p_T (>2 GeV/c) if nucleus-nucleus collisions were mere superpositions of nucleon-nucleon collisions. Any deviation observed from unity would indicate the presence of in-medium effects. Above $p_T = 2$ GeV/c, the $R_{\rm CP}$ of $\pi^{\pm}$, $p + \bar{p}$, K^0_S, and Λ, as measured by STAR, are found to be significantly lower than unity. This suggests a suppression of particle production at high p_T in central collisions relative to peripheral ones [17,18,37]. Theoretically, this is attributed to the energy loss of highly energetic partons while traversing through the dense medium created in heavy-ion collisions. We also observe that the $R_{\rm CP}$ of K^0_S and Λ differ. Since the mass of K^{*0} is close to that of baryons such as p and Λ, a comparison of $R_{\rm CP}$ of K^{*0} with those for K^0_S and Λ can be used to understand whether the observed differences in the $R_{\rm CP}$ of the K^0_S and the Λ are tied to the particle mass or the baryon-meson effect [17].

Figure 14 shows the K^{*0} $R_{\rm CP}$ as a function of p_T compared to those for Λ and K^0_S [17]. The shaded band around the data points represents the systematic uncertainties and the band around 1 on the right corner represents the normalization uncertainty. For Au + Au collisions at 200 GeV the K^{*0} $R_{\rm CP}$ was obtained from the p_T spectra of top 10% and 60–80% centrality classes. For Au + Au collisions at 62.4 GeV the p_T spectra of the top 20% and 60–80% centrality classes were

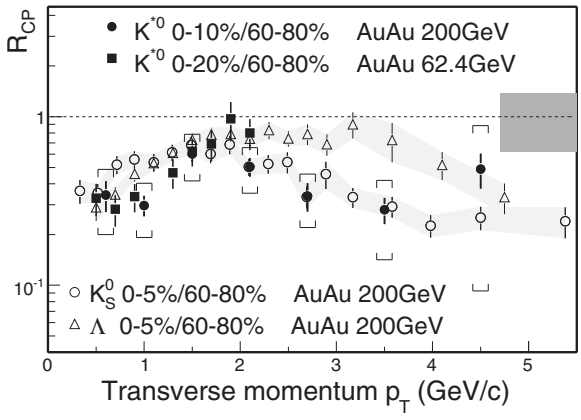

FIG. 14. The K^{*0} R_{CP} as a function of p_T in Au + Au collisions at 200 and 62.4 GeV compared to the R_{CP} of K^0_S and Λ at 200 GeV. The brackets around Au + Au 200 GeV data points are the systematic errors.

considered. The Λ and K^0_S R_{CP} correspond to the p_T spectra of the top 5% and 60–80% Au + Au collisions at 200 GeV [17]. For $p_T < 1.8$ GeV/c, the R_{CP} of K^{*0} in Au + Au collisions at 200 and 62.4 GeV are smaller than that of Λ and K^0_S. This is consistent with the assumption that the rescattering effect dominates over the regeneration effect for K^{*0} at low p_T. For Au + Au collisions at 200 GeV, for $p_T > 1.8$ GeV/c, the R_{CP} of K^{*0} is closer to that for K^0_S (differing from that of Λ). Since the masses of the Λ and K^{*0} are similar, the observed difference seems to be due to other than mass. The observed differences might arise because the Λ is a baryon, whereas K^{*0} is a meson. This supports the quark coalescence picture of particle production in the intermediate p_T range.

IV. SUMMARY

STAR has measured the K^{*0} resonance production at midrapidity in Au + Au and Cu + Cu collision systems at $\sqrt{s_{NN}} = 62.4$ and 200 GeV. A large sample of Au + Au collision data at $\sqrt{s_{NN}} = 200$ GeV enables us to extend the measurements to $p_T \sim 5$ GeV/c. The measured dN/dy and $\langle p_T \rangle$ of K^{*0} are higher at $\sqrt{s_{NN}} = 200$ GeV compared to the corresponding values at $\sqrt{s_{NN}} = 62.4$ GeV. For a given beam energy, the dN/dy and $\langle p_T \rangle$ are similar for Au + Au and Cu + Cu collisions at a given $\langle N_{\rm part} \rangle$. For $\sqrt{s_{NN}} = 62.4$ and 200 GeV the K^{*0} $\langle p_T \rangle$ is comparable to the same for protons, indicating that the $\langle p_T \rangle$ trends are dependent on the mass.

The $N(K^{*0})/N(K^-)$ ratio in central Au + Au collisions at both 62.4 and 200 GeV is much smaller compared to the respective values in $p + p$ collisions. The $N(\phi)/N(K^{*0})$ ratio in central Au + Au collisions at both 62.4 and 200 GeV is larger than that of $p + p$ collisions. While the increase in the $N(\phi)/N(K^{*0})$ ratio as a function of beam energy and collision centrality also suggests strangeness enhancement in heavy-ion collisions, other ratios indicates that heavy-ion collisions probably provide an environment with stronger rescattering of K^{*0} daughter particles relative to regeneration.

The large sample of Au + Au collision data at 200 GeV allow for a quantitative estimation of elliptic flow of K^{*0} and the interpretation of the v_2 in terms of a scaling based on the number of constituent quarks. The results support the quark coalescence model of particle production. More explicitly, K^{*0} are dominantly produced from direct quark combinations, with a negligible regenerated component. At low p_T, the nuclear modification factor for K^{*0} is seen to be similar for Au + Au collisions both at 62.4 and 200 GeV. At lower p_T, R_{CP} for Au + Au collisions at $\sqrt{s_{NN}} = 200$ GeV is lower than that for Λ and K^0_S, which is consistent with the observation that the rescattering effect dominates over regeneration effect. For $p_T > 1.8$ GeV/c, the K^{*0} R_{CP} in Au + Au collision at 200 GeV more closely follows that for K^0_S and at the same time differs from that for Λ. This also provides support for the quark coalescence picture at the intermediate p_T ranges studied.

ACKNOWLEDGMENTS

We thank the RHIC Operations Group and RCF at BNL, the NERSC Center at LBNL and the Open Science Grid consortium for providing resources and support. This work was supported in part by the Offices of NP and HEP within the US DOE Office of Science, the US NSF, the Sloan Foundation, the DFG cluster of excellence "Origin and Structure of the Universe" of Germany, CNRS/IN2P3, STFC, and EPSRC of the United Kingdom, FAPESP CNPq of Brazil, Ministry of Ed. and Sci. of the Russian Federation, NNSFC, CAS, MoST, and MoE of China, GA and MSMT of the Czech Republic, FOM and NWO of The Netherlands, DAE, BRNS, DST, and CSIR of India, Polish Ministry of Sci. and Higher Ed., Korea Research Foundation, Ministry of Sci., Ed. and Sports of the Republic of Croatia, Russian Ministry of Sci. and Tech., and RosAtom of Russia.

[1] J. Adams *et al.* (STAR Collaboration), Nucl. Phys. A **757**, 102 (2005).
[2] K. Adcox *et al.* (PHENIX Collaboration), Nucl. Phys. A **757**, 184 (2005).
[3] B. B. Back *et al.* (BRAHMS Collaboration), Nucl. Phys. A **757**, 28 (2005).
[4] I. Arsene *et al.* (PHOBOS Collaboration), Nucl. Phys. A **757**, 1 (2005).
[5] J. Schaffner-Bielich, Phys. Rev. Lett. **84**, 3261 (2000).
[6] R. Rapp and J. Wambach, Adv. Nucl. Phys. **25**, 1 (2000).
[7] B. I. Abelev *et al.* (STAR Collaboration), Phys. Rev. Lett. **97**, 132301 (2006).
[8] C. Adler *et al.* (STAR Collaboration), Phys. Rev. C **66**, 061901 (2002)(R).
[9] J. Adams *et al.* (STAR Collaboration), Phys. Rev. C **71**, 064902 (2005).

[10] R. Rapp and E. V. Shuryak, Phys. Rev. Lett. **86**, 2980 (2001).
[11] J. Adams *et al.* (STAR Collaboration), Phys. Rev. Lett. **92**, 092301 (2004).
[12] B. I. Abelev *et al.* (STAR Collaboration), Phys. Rev. Lett. **99**, 112301 (2007).
[13] M. Bleicher and J. Aichelin, Phys. Lett. B **530**, 81 (2002).
[14] S. D. Protopopescu *et al.*, Phys. Rev. D **7**, 1279 (1973).
[15] M. J. Matison *et al.*, Phys. Rev. D **9**, 1872 (1974).
[16] G. Torrieri and J. Rafelski, Phys. Lett. B **509**, 239 (2001).
[17] J. Adams *et al.* (STAR Collaboration), Phys. Rev. Lett. **92**, 052302 (2004).
[18] B. I. Abelev *et al.* (STAR Collaboration), Phys. Rev. Lett. **97**, 152301 (2006); Phys. Lett. B **655**, 104 (2007).
[19] D. Molnar and S. A. Voloshin, Phys. Rev. Lett. **91**, 092301 (2003).
[20] V. Greco, C. M. Ko, and P. Levai, Phys. Rev. Lett. **90**, 202302 (2003).
[21] C. Nonaka, B. Muller, M. Asakawa, S. A. Bass, and R. J. Fries, Phys. Rev. C **69**, 031902 (2004).
[22] B. I. Abelev *et al.* (STAR Collaboration), Phys. Rev. C **78**, 044906 (2008).
[23] K. H. Ackermann *et al.* (STAR Collaboration), Nucl. Inst. Methods A **499**, 624 (2003).
[24] M. Anderson *et al.*, Nucl. Inst. Methods A **499**, 659 (2003).
[25] C. Adler *et al.*, Nucl. Inst. Methods A **499**, 433 (2003); **461**, 337 (2001).
[26] B. I. Abelev *et al.* (STAR Collaboration), Phys. Lett. B **673**, 183 (2009).
[27] Particle Data Group, J. Phys. G **33**, 1 (2006).
[28] H. Bichsel, Nucl. Inst. Methods A **562**, 154 (2006); H. Bichsel, D. E. Groom, and S. R. Klein, Phys. Lett. B **592**, 242 (2004).
[29] B. I. Abelev *et al.* (STAR Collaboration), Phys. Rev. C **79**, 034909 (2009).
[30] D. Drijard *et al.*, Nucl. Inst. Methods A **225**, 367 (1984).
[31] D. L'Hôte, Nucl. Inst. Methods A **337**, 544 (1994).
[32] R. Brun *et al.*, GEANT3 User's Guide, CERN/DD/EE/84-1 (1984).
[33] M. Bleicher *et al.*, J. Phys. G: Nucl. Part. Phys. **25**, 1859 (1999).
[34] H. Zhang, Ph.D. thesis, Yale University, 2003.
[35] S. Dash, Ph.D. thesis, Homi Bhaba National Institute, 2010.
[36] G. Wilk and Z. Wlodarczyk, Phys. Rev. Lett. **84**, 2770 (2000).
[37] J. Adams *et al.* (STAR Collaboration), Phys. Lett. B **637**, 161 (2006); **616**, 8 (2005).
[38] T. Akesson *et al.*, Nucl. Phys. B **203**, 27 (1982).
[39] B. I. Abelev *et al.* (STAR Collaboration), Phys. Rev. C **79**, 64903 (2009).
[40] K. H. Ackermann *et al.* (STAR Collaboration), Phys. Rev. Lett. **86**, 402 (2001).
[41] A. M. Poskanzer and S. A. Voloshin, Phys. Rev. C **58**, 1671 (1998).
[42] X. Dong *et al.*, Phys. Lett. B **597**, 328 (2004).